SANDIA REPORT

SAND2011-6700
Unlimited Release
Printed October 2011

Pressure-shear experiments on granular materials

Tracy J. Vogler, C. Scott Alexander, Tom F. Thornhill, and William D. Reinhart

Prepared by
Sandia National Laboratories
Albuquerque, New Mexico 87185 and Livermore, California 94550

Sandia National Laboratories is a multi-program laboratory managed and operated by Sandia Corporation, a wholly owned subsidiary of Lockheed Martin Corporation, for the U.S. Department of Energy's National Nuclear Security Administration under contract DE-AC04-94AL85000.

Approved for public release; further dissemination unlimited.

Sandia National Laboratories

Issued by Sandia National Laboratories, operated for the United States Department of Energy by Sandia Corporation.

NOTICE: This report was prepared as an account of work sponsored by an agency of the United States Government. Neither the United States Government, nor any agency thereof, nor any of their employees, nor any of their contractors, subcontractors, or their employees, make any warranty, express or implied, or assume any legal liability or responsibility for the accuracy, completeness, or usefulness of any information, apparatus, product, or process disclosed, or represent that its use would not infringe privately owned rights. Reference herein to any specific commercial product, process, or service by trade name, trademark, manufacturer, or otherwise, does not necessarily constitute or imply its endorsement, recommendation, or favoring by the United States Government, any agency thereof, or any of their contractors or subcontractors. The views and opinions expressed herein do not necessarily state or reflect those of the United States Government, any agency thereof, or any of their contractors.

Printed in the United States of America. This report has been reproduced directly from the best available copy.

Available to DOE and DOE contractors from
U.S. Department of Energy
Office of Scientific and Technical Information
P.O. Box 62
Oak Ridge, TN 37831

Telephone: (865) 576-8401
Facsimile: (865) 576-5728
E-Mail: reports@adonis.osti.gov
Online ordering: http://www.osti.gov/bridge

Available to the public from
U.S. Department of Commerce
National Technical Information Service
5285 Port Royal Rd
Springfield, VA 22161

Telephone: (800) 553-6847
Facsimile: (703) 605-6900
E-Mail: orders@ntis.fedworld.gov
Online ordering: http://www.ntis.gov/help/ordermethods.asp?loc=7-4-0#online

SAND2011-6700
Unlimited Release
Printed October 2011

Pressure-shear experiments on granular materials

Tracy J. Vogler
Sandia National Laboratories
7011 East Ave.
M.S. 9042
Livermore, CA 94550

C. Scott Alexander, Tom F. Thornhill, and William D. Reinhart
Sandia National Laboratories
P.O. Box 5800
M.S. 1195
Albuquerque, NM 87185

Abstract

Pressure-shear experiments were performed on granular tungsten carbide and sand using a newly-refurbished slotted barrel gun. The sample is a thin layer of the granular material sandwiched between driver and anvil plates that remain elastic. Because of the obliquity, impact generates both a longitudinal wave, which compresses the sample, and a shear wave that probes the strength of the sample. Laser velocity interferometry is employed to measure the velocity history of the free surface of the anvil. Since the driver and anvil remain elastic, analysis of the results is, in principal, straightforward.

Experiments were performed at pressures up to nearly 2 GPa using titanium plates and at higher pressure using zirconium plates. Those done with the titanium plates produced values of shear stress of 0.1-0.2 GPa, with the value increasing with pressure. On the other hand, those experiments conducted with zirconia anvils display results that may be related to slipping at an interface and shear stresses mostly at 0.1 GPa or less. Recovered samples display much greater particle fracture than is observed in planar loading, suggesting that shearing is a very effective mechanism for comminution of the grains.

Acknowledgment

The authors wish to thank Heidi Anderson for her deft assembly of the targets as well as John Martinez and Robert (Rocky) Palomino for their efforts in the execution of the experiments. This work was supported through the Joint DoD/DOE Munitions Technology Development Program.

Contents

1 Introduction **7**

2 Experimental techniques **9**
2.1 Materials 9
2.2 Experimental Configuration 10
2.3 Instrumentation 12

3 Results **17**
3.1 Velocity Histories 17
3.2 Experiments with ZrO_2 Driver and Anvil 20
3.3 Strength 21
3.4 Post-Experiment Microscopy 23

4 Discussion **27**

5 Summary and Future Work **29**

References **31**

Appendix

A Tilt **35**

B VISAR Records **39**

Figures

1 SEM image of particles of the sand studied. The particles used in the pressure-shear experiments were obtained by sieving sizes of 50-90 μm from the as-received material shown here. 9
2 SEM image of the sieved WC powder used in this investigation. 10
3 Schematic of the target design used in the pressure-shear experiments. 11
4 The disassembled pressure-shear target showing the driver plate on the left and the anvil on the right. The gasket and sand sample can be seen on the anvil. The diameter of the right disk is 76 mm. 11
5 Schematic of the pressure shear experiment just prior to impact. 12
6 Projectile with inclined nosepiece. Two O-rings create a seal with the barrel, and the key engages the slot in the barrel to prevent the projectile from rotating. 13
7 Schematic of the VISAR setup to measure free surface velocities. The central probe sends the laser beam, and probes A and B receive the reflected light from the diffuse surface. 13
8 Assembled pressure-shear target mounted in gun. Four tilt pins are visible around the perimeter and three VISAR probes can be seen in the center. 14
9 X-t diagram for pressure-shear experiments showing wave propagation for the experiment. 18

10 Free surface velocity measurements for experiment ps-wc-1 from normal (0°) and off-axis (17° and 25°) probes. The time scale has been shifted so that the longitudinal wave arrives at the free surface at $t = 0$. 18
11 Normal and transverse velocities for the free surface of the anvil for experiment ps-wc-1. The time scale has been shifted so that the longitudinal wave arrives at the free surface at $t = 0$. 19
12 Normal and transverse velocities for the free surface of the anvil for experiment ps-egs-3, which was conducted with ZrO_2 impactor, driver, and anvil. The time scale has been shifted so that the longitudinal wave arrives at the free surface at $t = 0$. 20
13 Normal and transverse velocities for the free surface of the anvil for experiment ps-wc-4, which was conducted with ZrO_2 impactor, driver, and anvil. The time scale has been shifted so that the longitudinal wave arrives at the free surface at $t = 0$. 21
14 Strengths measured in pressure-shear experiments for sand and WC compared to pressure-shear measurements of Sairam and Clifton [1994] and inferred strength from penetration experiments of Holmquist and Johnson [2008]. 22
15 Strengths measured in pressure-shear experiments for sand and WC as a function of relative density. 23
16 SEM image for recovered granular WC from pressure-shear experiment wc-ti-1 in which the capsule remained intact through the experiment. Particles have been significantly fractured so that particle sizes are dramatically smaller than the original material shown in Fig. 2. 24
17 SEM image for recovered granular WC from a sample quasi-statically compressed to approximately 1.6 GPa [Vogler et al., 2007]. Most of the particles are nearly intact. 25
18 SEM image for recovered granular WC from a normal impact experiment in which the material was loaded to 4 GPa. Minimal fracture was seen with some breakage at particle corners so that the particles are similar to the original material shown in Fig. 2. 25

Tables

1 Properties of materials used for anvils in pressure-shear experiments. 10
2 Details of pressure-shear experiments on sand and granular WC. 17

1 Introduction

Sand and related soils are important because of their widespread presence on earth and other planetary bodies. Their dynamic behavior has been studied for conditions such as target response to penetration and interaction with explosions and blasts. The penetration of sands and soils by high-speed projectiles (e.g. [Allen et al., 1957; Bless et al., 2009; Cooper and Breaux, 2010; Forrestal and Luk, 1992]) and by shaped charge jets [Resnyansky and Wildegger-Gaissmaier, 2001] has been studied by several researchers. The behavior of sand and soils has also been studied within the context of seismic coupling of underground explosions [Lysne, 1970], cratering for planetary science applications [Cook and Mortensen, 1967; Housen and Holsapple, 2003], shallow landmines [Grujicic et al., 2006, 2008; Laine et al., 2002], and as a mitigator for blasts and fragments [Homae et al., 2007].

In order to model dynamic events of these types accurately, the material must be characterized for strain rates and pressures relevant to those events. While testing techniques for quasi-static conditions are well established [Mitchell and Soga, 2005], techniques for dynamic loading are less well developed. Recently, extensive work has been done with the split Hopkinson bar [Martin et al., 2009; Song et al., 2009] on wet and dry sand to strain rates of 500-1400 s^{-1}. Triaxial Hopkinson bar experiments have also been performed [Kabir et al., 2010]. The role of confining pressure was investigated by using different confining pressures or sleeves made of polyolefin, polycarbonate, and steel. To probe higher pressures and strain rates, Brown et al. [2007] conducted planar impact experiments to nearly 2 GPa. Strain rates in those experiments were of order 5×10^5 to 3×10^6 s^{-1}. However, planar impact conditions load the material in conditions that are nominally uniaxial strain, which means that the entire stress tensor is not known. Thus, additional measurements of the strength of the sand are needed to fully describe the response of the material.

To characterize the strength (deviatoric) behavior of materials at strain rates above those achievable with the Hopkinson bar, the pressure-shear (also referred to as oblique impact) experiment was developed [Clifton and Klopp, 1985; Gupta, 1976; Tang and Aidun, 2009]. As typically used, the experiment consists of a projectile with a planar nose inclined at an angle θ striking a planar target with the same inclination. The sample is a thin layer sandwiched between two plates in the target, and the experiment is designed so the impactor and plates, but not the sample, remain elastic. A slotted bore gun is used to ensure that the projectile does not rotate and the impact remains planar. This generates longitudinal and shear waves that propagate through the target and load the sample. The shear stress sustained by the sample is measured in a straightforward manner by measuring the velocity history of the back of the target.

The pressure-shear technique has been applied to a range of solid materials including aluminum [Yadav and Ramesh, 1998], hafnium [Yadav et al., 1995], tantalum [Duprey and Clifton, 2000], glass [Sundaram and Clifton, 1998], and SiC [Yuan et al., 2001]. In somewhat modified configurations, the technique has also been applied to measure the viscosity of fluids [Ramesh and Clifton, 1987] and friction at sliding interfaces [Yuan et al., 2009]. Although the pressure-shear technique has been used for a fairly wide range of materials and conditions, only Sairam and Clifton [1994] have used it to study granular materials. They studied Al_2O_3 powder to stress levels of about 2.5 GPa and found that the shear strength sustained was nearly linear with the applied normal stress.

In this report, we describe results from pressure-shear experiments on granular WC and silica sand. Conceptually, the experiments are similar to those of Sairam and Clifton [1994], though some modifications

were made to the experimental design. We have also succeeded in recovering some material for post-experiment characterization.

2 Experimental techniques

2.1 Materials

The sand studied in this investigation is a silica-based fine grain sand with grain sizes mainly between 150 and 450 μm. An SEM image of grains of this material is shown in Fig. 1. The material was quarried in Pensacola, Florida, washed and kiln-dried. It is designated as Quikrete #1961 and will be referred to herein as Eglin sand. Shock [Brown et al., 2007], Hopkinson bar [Martin et al., 2009; Song et al., 2009], and high-speed penetration [Cooper and Breaux, 2010] experiments have been performed on it. Additional information about Eglin sand can be found in these other references. In order to accommodate the thin sample needed for the pressure-shear experiments, the as-received sand was sieved to give particles over a size range of 50-90 μm. Such particles accounted for only a small percentage of the as-received material. Nevertheless, these results are considered to be applicable to the Eglin sand since only a modest degree of grain fracture is needed to change the as-received material to something similar to that used in these experiments.

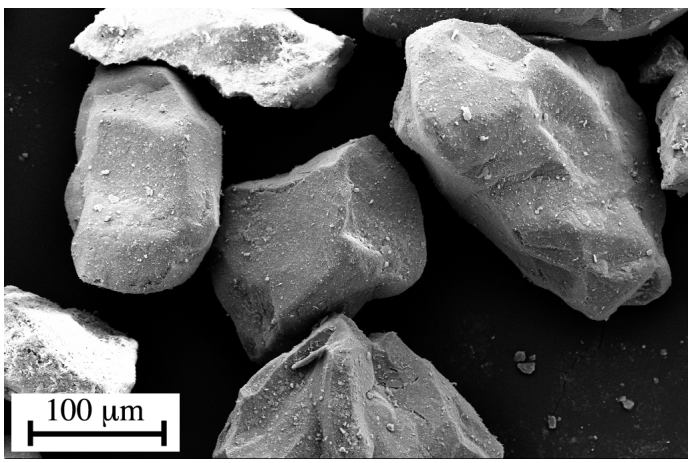

Figure 1. SEM image of particles of the sand studied. The particles used in the pressure-shear experiments were obtained by sieving sizes of 50-90 μm from the as-received material shown here.

The WC powder used in this investigation was a macro crystalline variety [Lassner and Schubert, 1999] produced by Kennametal Inc. of Latrobe, Pennsylvania. The particle morphology can be seen in Fig. 2. The grains are individual single crystals of varying sizes. The chemical composition of the Kennametal WC powder as provided by the manufacturer shows that the tungsten carbide is relatively pure and that there is little, if any, W_2C present. The WC crystal has a variant of the hexagonal close packed (HCP) structure, and its crystal density is 15.70 g/cm^3. Planar impact loading as well as quasi-static uniaxial strain compression have been performed on this material previously [Vogler et al., 2007]. As in that study, particles of nominal sizes of 20-32 μm were sieved from the as-received material.

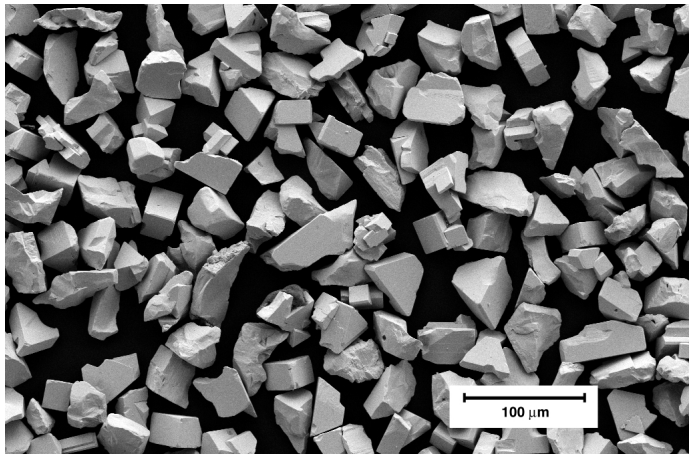

Figure 2. SEM image of the sieved WC powder used in this investigation.

2.2 Experimental Configuration

A 4" (101.6 mm) diameter bore gas gun using compressed helium was used to launch the projectiles. This gun differs from most smooth-bore gas guns in that the barrel includes a slot approximately 8 mm wide and 3 mm deep along its length to prevent the projectile from rotating. The gas gun was recently refurbished and modified to perform these experiments as described by Reinhart and Thornhill [2010].

The target used in the experiments is shown schematically in Fig. 3. It consists of two elastic plates with a thin sample sandwiched between them. The plates were either Ti-6Al-4V or partially stabilized ZrO_2. The yield strength of the Ti-6Al-4V has not been characterized but is assumed to be 1.28 GPa [Spletzer and Dandekar, 2001]. The yttria stabilized tetragonal ZrO_2 was made by Refractron Technologies and was found to have an Hugoniot elastic limit (HEL) of 17.6 GPa, which is close to the value measured previously for a similar material by Grady and Mashimo [1992]. This corresponds to a strength Y under uniaxial stress (assuming a von Mises yield surface) of 9.39 GPa. Specifics for the materials used as anvil materials are found in Table 1. Values shown for ZrO_2 were measured using ultrasonic techniques at Sandia, except for Y which was determined from the HEL from a plate impact experiment. Values for Ti-6Al-4V are taken from Spletzer and Dandekar [2001]. The ultrasonic velocities are believed to be representative of all Ti-6Al-4V, though the value of Y can depend upon heat treatment and impurity levels, among other things.

Table 1. Properties of materials used for anvils in pressure-shear experiments.

Material	ρ_o *(g/cm^3)*	C_L *(km/s)*	C_S *(km/s)*	ν	Y *(GPa)*
Ti-6Al-4V	4.415	6.12	3.17	0.317	1.28
ZrO_2	6.082	7.10	3.67	0.318	9.4

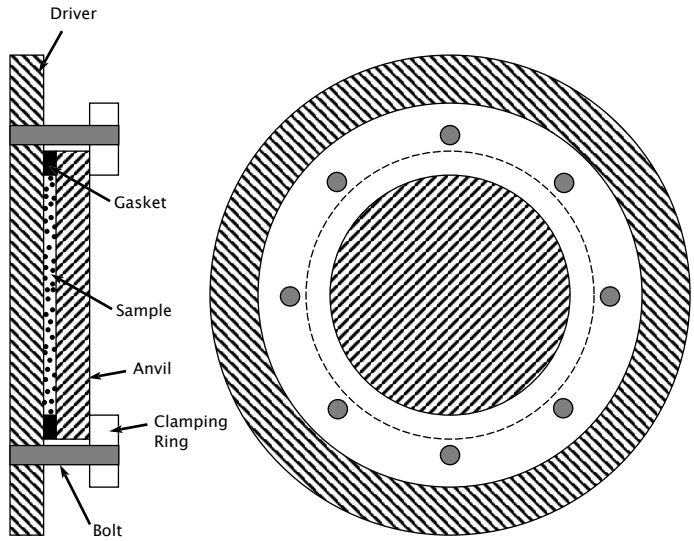

Figure 3. Schematic of the target design used in the pressure-shear experiments.

A gasket of nominal thickness 0.010 or 0.015" (254 or 381 μm) was placed between the plates to maintain the correct thickness for the sample. The inner diameter of the gasket was approximately 2.5" (64 mm). The anvil was clamped onto the driver plate so that the gasket was held in place, and the target was filled with powder through a groove cut in the anvil. The filling process was gradual and the target was agitated with a dental vibrator during filling to ensure that all the space was filled. A target that has been filled using this process and then opened is shown in Fig. 4.

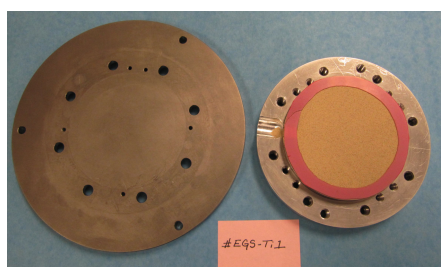

Figure 4. The disassembled pressure-shear target showing the driver plate on the left and the anvil on the right. The gasket and sand sample can be seen on the anvil. The diameter of the right disk is 76 mm.

After the target is assembled, it is mounted on the end of the gas gun and aligned to the angled nose of the impactor using an optical flat. Projectile velocity was measured through three shorting pins protruding from the side that are shorted out in sequence as the projectile passes. The primary diagnostic is VISAR or

PDV to measure the free surface velocity components as described in more detail in the following section. The projectile approaching the target is shown schematically in Fig. 5. The projectile, on which one can see the angled nose, the dual O-ring seal, and the key to engage the slot, is shown in Fig. 6.

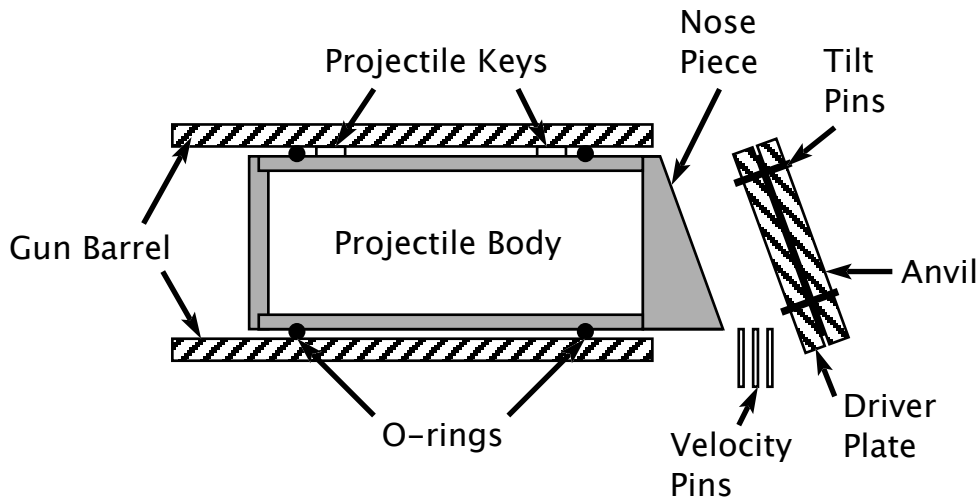

Figure 5. Schematic of the pressure shear experiment just prior to impact.

For experiments with ZrO_2 plates, a modified configuration was utilized. The driver and anvil had the same diameter and were initially glued together around the outer edge with the gasket in place. After being filled through the fill hole, this assembly was mounted flush into an aluminum target plate and epoxied into place. This design proved easier to mount into the gas gun and avoids the need for bolts into the driver, which would not be possible with a large ZrO_2 driver.

2.3 Instrumentation

Pressure-shear experiments require measurement of the free surface velocity of the back anvil plate, not only in the normal direction as is conventionally done in planar impact experiments but also in the transverse direction. One approach used has been the normal and transverse displacement interferometer [Kim et al., 1977]. While this approach has some advantages and works well at lower velocities, it is not suited to higher (100's of meters per second) free surface velocities. An alternate approach is the use of the laser velocity interferometry system known as VISAR [Barker and Hollenbach, 1972] with multiple off-axis measurements to resolve the two velocity components [Chhabildas et al., 1979]. In this investigation, we use a modified version of the configuration of Chhabildas *et al.* as shown schematically in Fig. 7. A single probe oriented so as to be normal to the anvil surface illuminates it. The surface is diffused somewhat so that some of the light is scattered away from the normal and received by probes arranged at 17° off normal in one direction and 25° off normal in the other. The measurements made with these probes are analyzed in the same way as standard VISAR measurements [Dolan, 2006]. The apparent velocities measured, v_A and v_B, are related to the normal and transverse velocities, v_x and v_y, through

Figure 6. Projectile with inclined nosepiece. Two O-rings create a seal with the barrel, and the key engages the slot in the barrel to prevent the projectile from rotating.

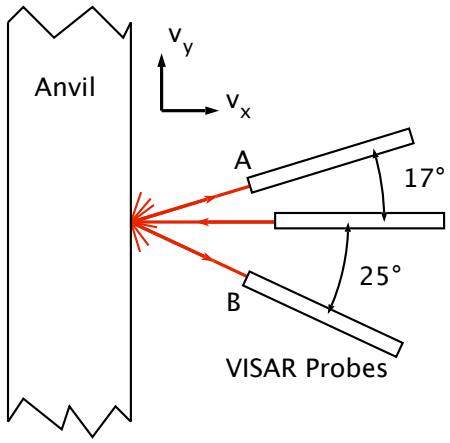

Figure 7. Schematic of the VISAR setup to measure free surface velocities. The central probe sends the laser beam, and probes A and B receive the reflected light from the diffuse surface.

$$v_A = \frac{\cos 17 + 1}{2} v_x + \frac{\sin 17}{2} v_y, \tag{1}$$

and

$$v_B = \frac{\cos 25 + 1}{2} v_x - \frac{\sin 25}{2} v_y. \tag{2}$$

These equations can be readily inverted to determine the normal and transverse velocities of interest. One can see that as the angles increase the measurement becomes more sensitive to the quantity of interest, v_y. However, the angles cannot become too large or insufficient light will be returned for the VISAR to operate. In addition to the A and B probes, a separate VISAR probe was fielded in the normal direction to measure v_x independently. In some experiments, the orientation of the two off-axis probes was opposite that shown in the figure, but the changes in the analysis for that case are minimal.

In addition to the VISAR probes, four self-shorting pins were arranged circumferentially around the target to measure the tilt of the impactor relative to the target. The assembled target with the VISAR probes and the tilt pins in shown in Fig. 8.

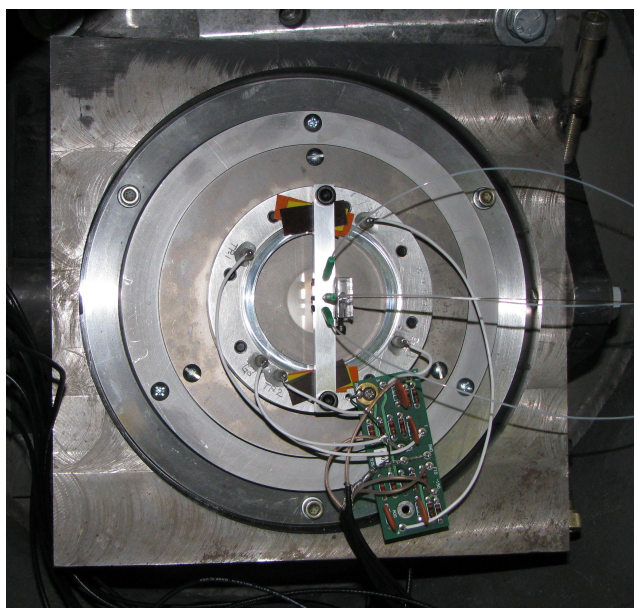

Figure 8. Assembled pressure-shear target mounted in gun. Four tilt pins are visible around the perimeter and three VISAR probes can be seen in the center.

Attempts were made to utilize photon doppler velocimetry (PDV) [Dolan, 2010; Strand et al., 2006]. In principal, PDV should be well suited to pressure-shear experiments because of the potential for low light

return in the angled probes. However, due to the angled ends on the fiber probes and the wavelength used being outside the visible range, it proved difficult to achieve proper alignment of the probes to receive light from the illuminated region of the target. Modifications to the PDV system will likely be needed to make it suitable for these experiments.

This page intentionally left (almost) blank.

3 Results

A series of experiments were conducted on the sand and WC powder described in Section 2.1. Details of these experiments are given in Table 2. The values of normal stress, σ, shown in the table are calculated as

$$\sigma = \frac{1}{2}\rho_o^{anv} C_L^{anv} V_x, \tag{3}$$

where ρ_o is the initial density, C_L is the longitudinal sound speed, and V_x is the normal velocity of the free surface, which will be equal to the impact velocity for symmetric impact such as used here. The superscript *anv* denotes properties of the anvil (Ti-6Al-4V or ZrO_2). The calculation of τ and $\dot{\gamma}$ are described below.

Table 2. Details of pressure-shear experiments on sand and granular WC.

Expt.	*Material*	*Anvil Matl.*	θ	V_{impact} *(m/s)*	σ *(GPa)*	τ *(GPa)*	$\dot{\gamma}$ *(s^{-1})*
ps-egs-1	sand	Ti-6Al-4V	20°	118	1.50	0.18	3.5×10^4
ps-egs-2	sand	Ti-6Al-4V	20°	78	1.00	0.15	1.2×10^4
ps-egs-3	sand	ZrO_2	20°	106	2.00	?	?
ps-egs-5	sand	ZrO_2	20°	66	1.40	0.04	4.9×10^4
ps-wc-1	WC	Ti-6Al-4V	20°	121	1.50	0.11	9.8×10^5
ps-wc-2	WC	Ti-6Al-4V	20°	145	1.85	0.22	7.0×10^5
ps-wc-3	WC	Ti-6Al-4V	20°	66	0.85	0.09	3.4×10^5
ps-wc-4	WC	ZrO_2	20°	79	1.60	0.08	8.0×10^5
ps-wc-6	WC	ZrO_2	20°	129	2.59	0.09	1.4×10^6

When the impactor strikes the driver plate, it generates two waves in the driver: a compressive wave travelling at a velocity near C_L and a shear (distortional) wave travelling at a velocity near C_S as shown in Fig. 9. The longitudinal wave reaches the sample, compressing it. The wave then reverberates between the driver and the anvil until the sample reaches the stress level given by Eq. 3. The shear wave arrives somewhat after the longitudinal wave and begins to shear the sample. Some fraction of the shear wave is transmitted by the sample into the anvil, and eventually it reaches the free surface. The transverse velocity, v_y, beginning at this time is the primary experimental quantity of interest. When the longitudinal wave reflected from the anvil free surface reaches the sample (denoted in the figure as "sample unloaded"), the normal stress in the sample goes to zero. This will likely change the shear stress that can be sustained by the sample significantly, so when the shear wave transmitted at this time (shown by the purple dashed line) reaches the free surface the experiment is, effectively, over.

3.1 Velocity Histories

In each experiment, velocity measurements were made at the free surface of the anvil as described in Section 2.3. Velocity measurements for a typical experiment, ps-wc-1, are shown in Fig. 10. One interesting aspect

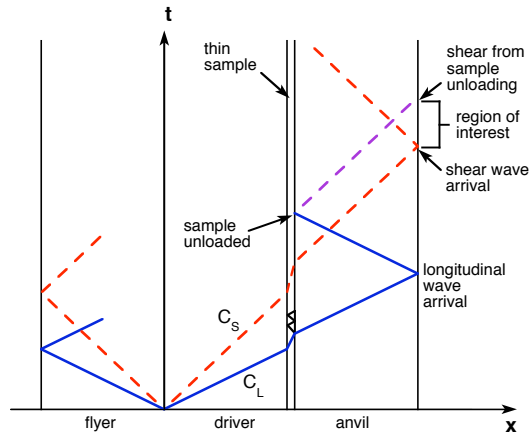

Figure 9. X-t diagram for pressure-shear experiments showing wave propagation for the experiment.

of these histories is that the longitudinal wave takes approximately 1 μs to reach the equilibrium value given in Eq. 3. This is due to two effects. First, waves in granular materials such as sand and WC have finite rise times if the stress level is low or moderate [Brown et al., 2007; Vogler et al., 2007]. Second, because the WC powder has a lower impedance than the Ti-6Al-4V driver and anvil, the longitudinal wave reverberates within the sample until the equilibrium stress level is reached.

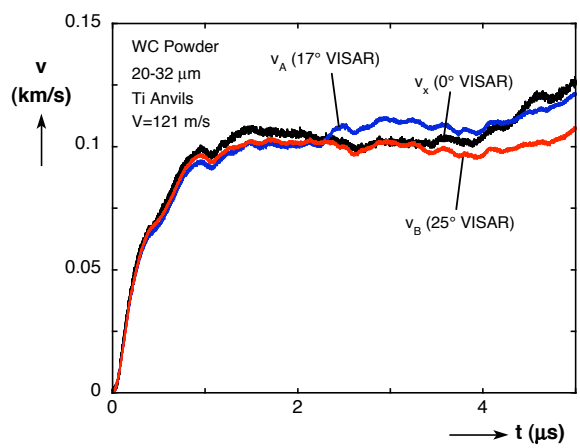

Figure 10. Free surface velocity measurements for experiment ps-wc-1 from normal (0°) and off-axis (17° and 25°) probes. The time scale has been shifted so that the longitudinal wave arrives at the free surface at $t = 0$.

By inverting Eqns. 1 and 2, one can obtain v_x and v_y. These velocity histories are shown for the same experiment in Fig. 11. First, one notes that the two different measurements of v_x from the normal (0°) probe and as found from v_A and v_B agree quite well with one another, at lease until around 2.2 μs. This is a valuable check of the off-normal velocity measurements and indicates the technique is working as expected. The second observation is that $v_y \neq 0$, even for times well before the arrival of the shear wave at the free surface. Although this was quite puzzling at first, it was determined that this transverse velocity is due to tilt of the impactor relative to the target. The issue of tilt is discussed thoroughly in Appendix A. Here, we merely point out that the tilt is modest, the value of v_y at early times is about what would be expected based on the measured tilt, and the value of v_y after the arrival of the shear wave is unaffected by the tilt. Third, the shear wave is seen to arrive at approximately t = 2.25 μs, and v_y takes approximately 0.25 μs to reach a steady state. It is around this time that the two measurements of v_x diverge from one another somewhat, though it is not clear why they should do so. The value of v_y reached, around 17 m/s, can be used to calculate the shear stress in the sample from

$$\tau = \frac{1}{2}\rho_o^{anv} C_S^{anv} v_y. \tag{4}$$

In this case, a shear stress of 0.11 GPa is found. Values of shear stress for the other experiments can be found in Table 2.

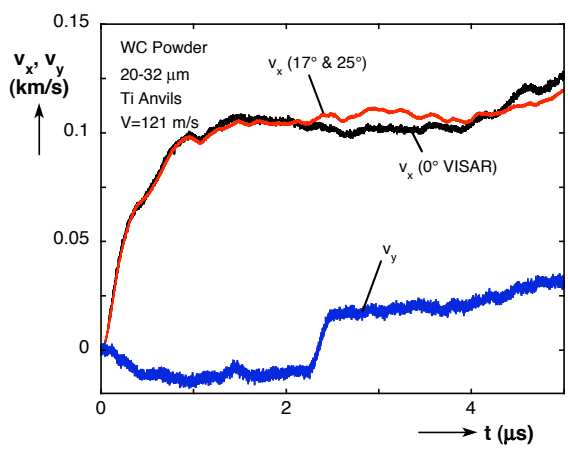

Figure 11. Normal and transverse velocities for the free surface of the anvil for experiment ps-wc-1. The time scale has been shifted so that the longitudinal wave arrives at the free surface at $t = 0$.

From the velocity histories, one can also estimate the strain rate in the sample using [Ramesh and Clifton, 1987]

$$\dot{\gamma} = \frac{V_{impact} sin\theta - v_y}{h}, \tag{5}$$

where h is the sample thickness. In principal, h should be interpreted as the current (compressed) sample thickness, but in practice the initial nominal thickness (250 or 381 μm) provides a sufficiently accurate estimate that should be a lower bound on the actual strain rate. Values for strain rate calculated using Eq. 5 with the initial sample thicknesses are given in Table 2.

3.2 Experiments with ZrO_2 Driver and Anvil

Although the experiments with Ti-6Al-4V anvils gave results that appear reasonable, the strength of titanium is too low to be useful for the entire pressure range of interest. Previous experiments by Clifton and coworkers utilized WC plates (c.f. [Duprey and Clifton, 2000; Frutschy and Clifton, 1998; Grunschel and Clifton, 2007]). While WC has a higher elastic limit than titanium, it is still only about 5 GPa. Some other ceramics such as SiC, B_4C, and sapphire have values for the Hugoniot Elastic Limit (HEL) above 10 GPa. However, they also have very high wave speeds in excess of 10 km/s that would significantly limit the duration of the experiment before the arrival or release waves from a front, back, or edge surface. ZrO_2 has a high elastic limit and relatively low wavespeeds, apparently making it a nearly ideal anvil material for pressure-shear experiments.

Experiments were conducted on both sand and WC utilizing ZrO_2 plates as impactors, drivers, and anvils as shown in Table 2. Impact velocities were chosen so as to overlap the results using titanium plates as well as to extend the pressure levels. Representative velocity histories are shown in Figs. 12 and 13 for sand and WC, respectively.

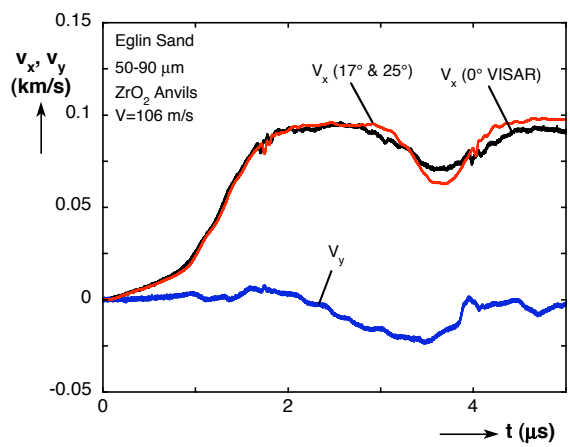

Figure 12. Normal and transverse velocities for the free surface of the anvil for experiment ps-egs-3, which was conducted with ZrO_2 impactor, driver, and anvil. The time scale has been shifted so that the longitudinal wave arrives at the free surface at $t = 0$.

The resolved velocity histories for experiment ps-egs-3 (Fig. 12), which utilized ZrO_2 plates, differs from the experiments in which titanium plates were used in that there is no distinct arrival of a shear wave.

Though transverse velocities from nearly zero to about 25 m/s are observed, there is no obvious velocity value one can pick to associate with the shear of the sample. The other sand experiment with ZrO_2 had a negligible transverse velocity.

Unusual features are seen in the resolved velocity histories for experiments with ZrO_2 plates and WC powder as shown in Fig. 13. Around the time of the expected arrival of the shear wave, a drop in the longitudinal velocity and rapid oscillations in both velocity components occur. This behavior was observed in both ps-wc-4 and ps-wc-6. While its origin is not known, it may be that there is sliding at an interface. After the oscillatory behavior a relatively stable transverse velocity is observed. However, the resulting shear stress is lower for these two experiments than would be expected based upon the results with the titanium plates.

Because of the unexplained behavior in the experiments with ZrO_2, values for shear stress and strain rates in Table 2 should be viewed with extreme caution.

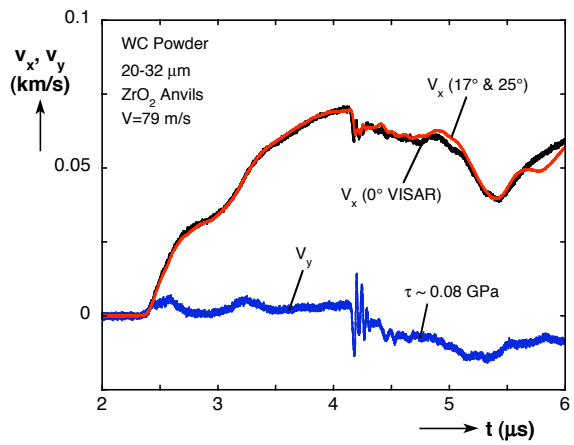

Figure 13. Normal and transverse velocities for the free surface of the anvil for experiment ps-wc-4, which was conducted with ZrO_2 impactor, driver, and anvil. The time scale has been shifted so that the longitudinal wave arrives at the free surface at $t = 0$.

3.3 Strength

In order to compare the shear stresses measured in the experiments with titanium anvils to the conventional measure of strength, the flow stress under uniaxial stress Y, we assume that the material exhibits a von Mises flow behavior. Further, we assume that when the material is sufficiently deformed in shear that $\sigma_{xx} = \sigma_{yy} = \sigma_{zz} = P$, where σ is the component of stress (positive in compression) and P the pressure. The flow stress is then given by

$$Y = \sqrt{3}\tau. \tag{6}$$

The assumption that the normal stresses are all equal can readily be demonstrated to be correct for a Prandtl-Reuss elastic-plastic material [Hill, 1950] and is probably reasonable for most metals. However, the validity of the assumption for granular materials is deserving of further examination. Values of Y for sand and granular WC are shown in Fig. 14 as a function of σ_{xx} assumed equal to pressure. Strengths for both materials increase with pressure, with a linear fit plausible for both materials. It is interesting that the strength of sand is greater than that of WC, which is a surprising result given the perceived strength and toughness of the latter. An explanation of this result is offered below.

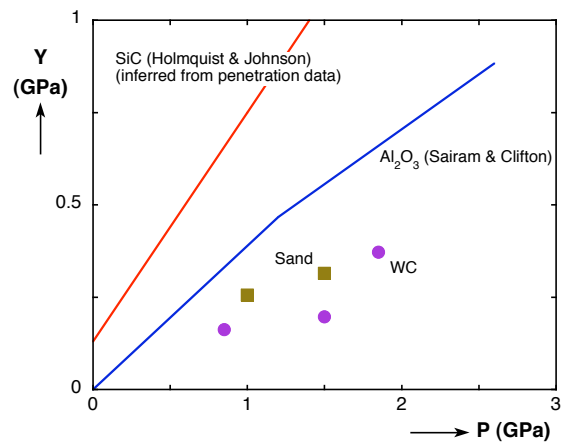

Figure 14. Strengths measured in pressure-shear experiments for sand and WC compared to pressure-shear measurements of Sairam and Clifton [1994] and inferred strength from penetration experiments of Holmquist and Johnson [2008].

For comparison, the results of Sairam and Clifton [1994] for Al_2O_3 are also shown. The strengths they found are similar, though somewhat higher than the current results. This may be due to the much smaller grain size of their material, approximately 0.4 μm or two to three orders of magnitude smaller than the initial particle sizes for sand and WC. Such small particles would be less likely to fracture, perhaps leading to higher strengths. Also shown for comparison are the results of Holmquist and Johnson [2008] for granular SiC as determined by fitting model parameters for high-velocity penetration experiments. Their material had a particle size of 1-3 μm, and was compressed to $\sim$71% initial density. Although both a smaller particle size and a higher initial density should tend to give the granular SiC higher strength, neither seems likely to explain the much higher strengths their results suggest. One possible explanation is that their results depend upon the constitutive model chosen so that a model with an alternate functional form might give significantly different results. Peak strain rates in the penetration experiments are much higher than in the current experiments, though a full range of strain rates from the peak rate to zero occurs in the penetration experiments. It is also possible that the underlying assumption that the normal stress are equal is fundamentally incorrect for granular materials, which would make a comparison with the current pressure-shear data or that of Sairam and Clifton [1994] invalid. Finally, there may be a dependence upon the third

invariant of stress that is not captured by the von Mises yield surface [Brannon, 2007].

Presenting strength as a function of pressure does not convey all aspects of material behavior, so in Fig. 15 the same strength values are plotted against the relative density of the material from the previously measured Hugoniot for these powders [Brown et al., 2007; Vogler et al., 2007]. To do this, a fit to the Hugoniot data is used to determine the compressed density based on the final equilibrium stress given in Table 2. This neglects any possible differences between loading through a single step and multi-step loading such as those observed for granular WC [Vogler et al., 2007], but it still should provide a reasonably accurate measurement of density. When plotted in this manner, the WC is seen to be significantly stronger than the sand because the sand compacts much more easily. Unfortunately, Sairam and Clifton [1994] did not measure the compaction response of their Al_2O_3, and [Holmquist and Johnson, 2008] provide only a density measurement at a single stress level.

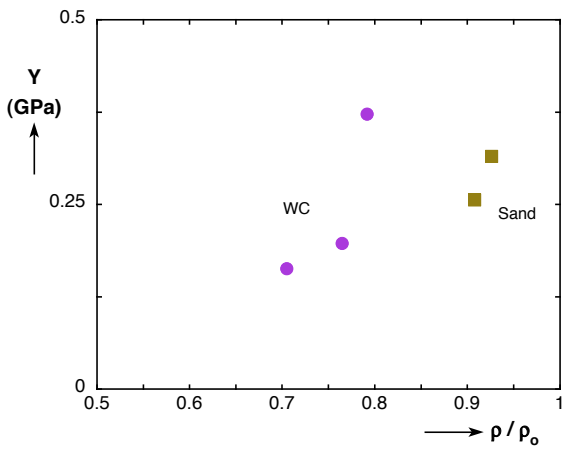

Figure 15. Strengths measured in pressure-shear experiments for sand and WC as a function of relative density.

3.4 Post-Experiment Microscopy

In most of the experiments reported here, the target broke open during the experiment. However, in one of the experiments (ps-wc-1) the bolts did not break and the target was recovered intact. This experiment experienced a peak equilibrium pressure of approximately 1.5 GPa. Although some of the WC powder leaked out through the fill hole, some of it remained between the titanium plates. While the target could not be said to be recovered in a ”soft” manner, most of the energy was absorbed by soft cushioning material (old parachutes). Thus, it probably experienced its most extreme loading during the initial impact event, and the material recovered is probably reasonably representative of the material that results from the initial pressure-shear loading.

After cutting the bolts to open the target, the WC powder remaining on the anvil was examined using a scanning electron microscope; a representative image is shown in Fig. 16. The material is obviously very

different from the original 20-32 μm powder shown in Fig. 2 with most of the particles 2-3 μm or less in size and many of them in the sub-micron range. In this image, a couple of particles with a size on the order of 10 μm are also visible. Thus, it is apparent that the material has undergone a great deal of comminution to reduce the particle size by one to two orders of magnitude.

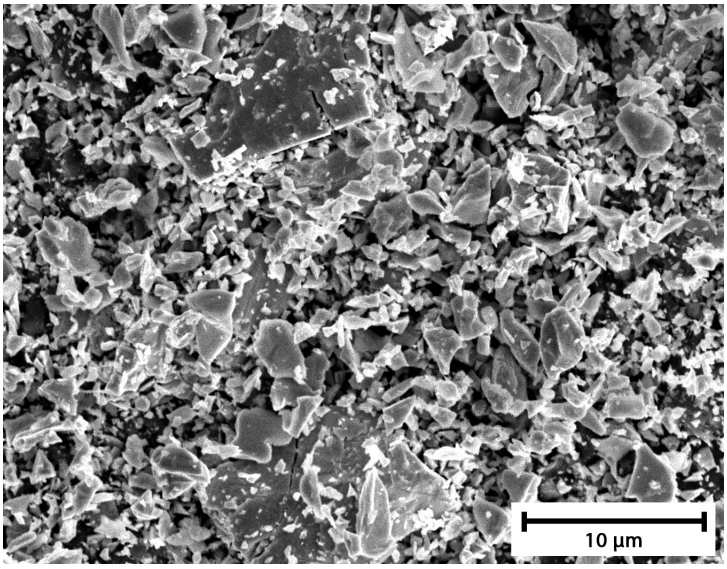

Figure 16. SEM image for recovered granular WC from pressure-shear experiment wc-ti-1 in which the capsule remained intact through the experiment. Particles have been significantly fractured so that particle sizes are dramatically smaller than the original material shown in Fig. 2.

The material shown in Fig. 16 experienced both longitudinal and shear loading, and it is not immediately obvious which of the two resulted in the comminution of the grains. Material loaded quasi-statically in uniaxial strain to approximately 1.6 GPa [Vogler et al., 2007] was found to be moderately fragmented with most of the particles nearly intact except for small particles broken off of corners and edges as shown in Fig. 17. To examine the effect of longitudinal dynamic loading on particle size, a capsule filled with WC powder was impacted by a Lexan (polycarbonate) projectile at 1.06 km/s. The capsule was fabricated from 304 stainless steel and surrounded radially by Macor ceramic that helps to reduce the effects of converging release waves from the boundaries. This impact resulted in an initial stress of approximately 1 GPa in the powder and an equilibrated stress of approximately 4 GPa. An SEM image of the recovered material is shown in Fig. 18. Clearly, this material looks more like the material uniaxially tested in quasi-static loading as shown in Fig. 17 and quite different from that loaded in pressure-shear. Thus, it seems that shearing is much more effective at comminuting the powder than uniaxial compression.

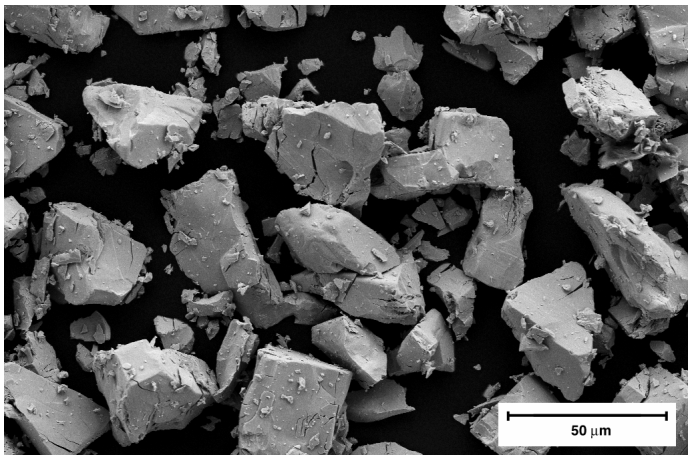

Figure 17. SEM image for recovered granular WC from a sample quasi-statically compressed to approximately 1.6 GPa [Vogler et al., 2007]. Most of the particles are nearly intact.

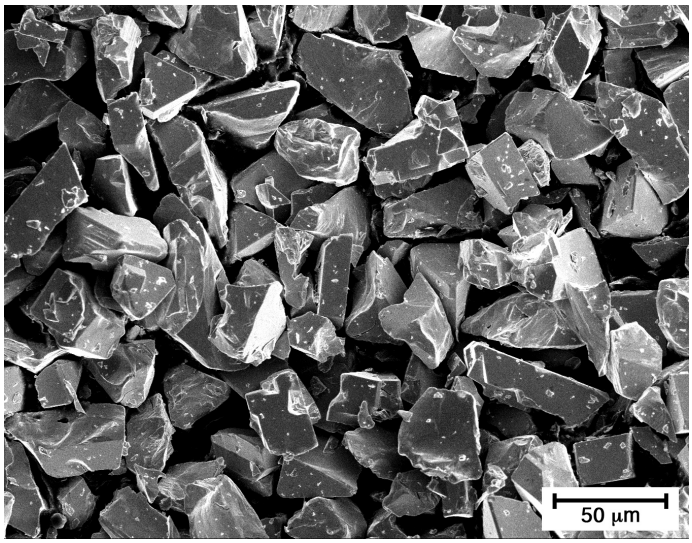

Figure 18. SEM image for recovered granular WC from a normal impact experiment in which the material was loaded to 4 GPa. Minimal fracture was seen with some breakage at particle corners so that the particles are similar to the original material shown in Fig. 2.

This page intentionally left (almost) blank.

4 Discussion

The results presented in Section 3 represent some of the first results for pressure-shear experiments on granular materials. For experiments with titanium plates, well-defined shear waves are observed that can be used to obtain a shear stress. The shear stresses obtained appear plausible, though there is very little data in this regime with which to compare. We note that in some unpublished integrated experiments involving relatively low pressures, strengths of the order of 0.1 GPa were inferred for granular WC. While the sand initially appeared to be stronger than the WC, which would be surprising, sand is found to be nearly fully compacted while the WC still retains significant porosity. For comparable compaction levels, WC will clearly be stronger than sand.

The strengths for sand and WC are somewhat lower than those found for Al_2O_3 by Sairam and Clifton [1994]. The initial particle size of their Al_2O_3 particles was two to three orders of magnitude smaller than those studied here, which could explain this difference somewhat as very small particles would be expected to be stronger. On the other hand, the recovered particles mainly had sizes around that level, so no clear conclusion can be drawn. The other complication is that the degree of compaction can strongly affect the strength as shown in Fig. 15. Unpublished compaction data on Al_2O_3, albeit on significantly larger initial sizes, suggests that its compaction response is close to that of WC. A possible explanation is that the comminution process of the WC and sand during shearing results in the lower strength values compared to those for Al_2O_3. If that is correct, then WC initial particles that are sub-micron would be expected to be significantly stronger than that studied here since the comminution process would largely be absent.

In order to develop a constitutive model for a material such as sand that is accurate over a wide range of conditions, one will need to obtain data from multiple experimental techniques covering quasi-static (uniaxial strain or triaxial), intermediate rate (Hopkinson bar), and high rate (pressure-shear or planar impact) regimes. Previous work comparing Hopkinson bar data to quasi-static results suggests the strain rate effects in sand are small [Song et al., 2009]. Similarly, comparison of planar impact and quasi-static uniaxial strain experiments [Vogler et al., 2011] also indicates little strain rate dependence.

Experiments with sleeves of different stiffnesses [Song et al., 2009] such as polyolefin and steel show that the confinement (i.e., the pressure) plays an important role in behavior. This was examined in more detail by Kabir et al. [2010] in triaxial Hopkinson bar experiments. Indeed, the current results demonstrate the ability of the sand to transmit a shear stress is a function of pressure. All of the triaxial Hopkinson bar experiments were conducted at significantly lower pressures than those reported herein, making a direct comparison impossible. Further, the stress in the triaxial Hopkinson bar experiments display a principal stress difference that rises with strain up to the 12% that was reached in the experiments. This is most pronounced in the experiments with the higher confinement pressures. Kabir et al. [2010] chose to plot their measured stress differences at 7% strain, but this choice is entirely arbitrary. Thus, one cannot say that anything akin to a steady flow stress was achieved in the triaxial Hopkinson bar experiments. Even so, a stress difference of over 0.4 GPa was found at $\dot{\varepsilon} = 1000s^{-1}$ for a confining stress of 0.15 GPa. Such a value is much higher than the strength data shown in Fig. 14 and cannot readily be reconciled with it. One possible explanation is the concept of a failure envelope giving the strength of the intact material and a failed strength that is significantly lower as used by Holmquist and Johnson [2008] in their JHB and JH-1 models. Under this interpretation, the experiments by Kabir et al. [2010] reveal the behavior of ”intact” sand whereas the present pressure-shear experiments probe the ”failed” material. A second possibility is that the interpretation of the stress state in the pressure-shear experiments as a hydrostatic pressure with a

superimposed shear stress is not valid. Such an interpretation would be correct under classical plasticity, but for a material such as sand it may not be valid. Finally, it is possible that interpreting the triaxial Hopkinson bar in the same manner as conventional triaxial experiments is incorrect. In any event, additional study is merited to understand how the triaxial Hopkinson bar and the pressure-shear data relate to one another.

The recovered WC powder that has undergone shear shows dramatically different particle sizes compared to the original 20–30 μm material and to the material that material that was compressed to 1.6 GPa statically or 4 GPa dynamically. Examination of the X-t diagram indicates that the shear release waves do not reach the sample until after it has undergone shearing for several microseconds. Shearing of the sample for 5 μs, as will occur for titanium plates, at the rates given in Table 2 gives shear strains of order 1.7-5, much larger than the strains associated with compression. Thus, the greater comminution due to shearing may be largely due to the greater deformation possible under that mode. The shearing of granular and comminuted material seems to play an important role in penetration phenomena [Cooper and Breaux, 2010; Shockey et al., 1990], and the deformation of thin layers of granular materials has been shown to be important in explosively loaded granular and fully dense ceramics [Nesterenko et al., 1996; Shih et al., 1998a,b].

Although the experiments using titanium plates were successful, those in which ZrO_2 plates were used gave ambiguous or confusing results. The most likely explanation is slipping at one or both of the powder/plate interfaces. Such behavior would probably not be expected for the titanium plates where the hard ceramic particles could ”bite” into the softer metal plates. Though we have not measured the nanoindentation of the ZrO_2, a conventional hardness of 13 GPa is reported by the manufacturer. This is not as hard as WC but harder than the sand. Since nanoindentation will give higher hardness values, the viewpoint of ZrO_2 intermediate to the other two materials seems reasonable. Thus, sand may merely slide over the smooth surface of the plates, while WC might scratch or become imbedded in them to some degree though not as much as it embeds into titanium. The velocity records in Fig. 13 are suggestive of a stick-slip response, and the transverse velocity seen at later times may be indicative of dynamic sliding on a rough surface. Both of these phenomena would be consistent with a small amount of ”bite” of the WC into the ZrO_2. The friction of granular materials with metals or ceramics may itself be an important aspect for penetrators, so additional study of sliding behavior would likely be of interest on its own.

5 Summary and Future Work

Pressure-shear experiments have been conducted successfully on granular WC and silica sand. The samples are found to transmit shear stresses of 0.1-0.2 GPa, and recovered samples are dramatically comminuted with much smaller particle sizes. Attempts to utilize ZrO_2 plates so that higher pressures could be reached gave results that were ambiguous but suggestive of sliding at sample/plate interfaces.

While these initial results are promising, additional work remains to be done on the pressure-shear technique in general and its use for granular materials in particular. Some of the main items are:

- Utilize ZrO_2 plates for experiments on simpler materials such as aluminum. Such results could be compared to literature values to gain confidence in the use of this material as a pressure-shear anvil.
- Perform experiments on WC and sand with tool steel plates. Because of its higher strength, tool steel should allow higher pressures to be reached while providing an interface that is less likely to slip.
- Examine the effect of particle size by testing WC with much smaller initial particles. It would also be of interest to obtain data for an Al_2O_3 similar to that of Sairam and Clifton [1994].
- The dynamic compaction of wet sand has been studied as has its behavior in a Hopkinson bar. How a small amount of water will affect the pressure-shear behavior of sand or WC is unknown.
- In principal, PDV should be well suited to pressure-shear experiments because of its ability to function even at very low light returns. However, modifications to the probes will likely be needed in order to obtain good results with the PDV in pressure-shear experiments.
- A better understanding of the errors and uncertainties associated with pressure-shear experiments is needed. The consistency observed for multiple experiments on the same material suggests a modest uncertainty, but further examination of the experimental setup as well as replicate experiments should help establish the error bars that are appropriate for the strengths obtained from these experiments.

This page intentionally left (almost) blank.

References

Allen, W.A., Mayfield, E.B., Morrison, H.L., 1957. Dynamics of a projectile penetrating sand. Journal of Applied Physics 28, 370–376.

Barker, L.M., Hollenbach, R.E., 1972. Laser interferometry for measuring high velocities for any reflecting surface. Journal of Applied Physics 43, 4669–4675.

Bless, S.J., Berry, D.T., Pedersen, B., Lawhorn, W., 2009. Sand penetration by high-speed projectiles. In: Elert, M.L., Buttler, W.T., Furnish, M.D., Anderson, W.W., Proud, W.G. (Eds.), Shock Compression of Condensed Matter - 2009. AIP, New York, pp. 1361–1364.

Brannon, R.M., 2007. Elements of phenomonological plasticity: geometrical insight, computational algorithms, and topics in shock physics. In: Horie, Y. (Ed.), Shock Wave Science and Technology Reference Library. Vol. 2. Springer, Berlin, pp. 225–274.

Brown, J.L., Vogler, T.J., Grady, D.E., Reinhart, W.D., Chhabildas, L.C., Thornhill, T.F., 2007. Dynamic compaction of sand. In: Elert, M., Furnish, M.D., Chau, R., Holmes, N., Nguyen, J. (Eds.), Shock Compression of Condensed Matter-2007. AIP, New York, pp. 1363–1366.

Chhabildas, L.C., Sutherland, H.J., Asay, J.R., 1979. A velocity interferometer technique to determine shear-wave particle velocity in shock-loaded solids. Journal of Applied Physics 50, 5196–5201.

Clifton, R.J., Klopp, R.W., 1985. Pressure-shear plate impact testing. In: Metals Handbook, Volume 8, 9th Edition. American Society for Metals, Metals Park, Ohio, pp. 230–239.

Cook, M.A., Mortensen, K.S., 1967. Impact cratering in granular materials. Journal of Applied Physics 38, 5125–5128.

Cooper, W.L., Breaux, B.A., 2010. Grain fracture in rapid particulate media deformation and a particulate media research roadmap from the PMEE workshops. International Journal of Fracture 162, 137–150.

Dolan, D.H., 2006. Foundations of VISAR analysis. Sandia National Laboratories, Report SAND2006-1950.

Dolan, D.H., 2010. Accuracy and precision in photonic doppler velocimetry. Review of Scientific Instruments 81, 053905.

Duprey, R.C., Clifton, R.J., 2000. Pressure-shear response of thin tantalum films. In: Furnish, M.D., Chhabildas, L.C., Hixson, R.S. (Eds.), Shock Compression of Condensed Matter-1999. AIP Press, pp. 447–450.

Forrestal, M.J., Luk, V.K., 1992. Penetration into soil targets. International Journal of Impact Engineering 12, 427–444.

Frutschy, K.J., Clifton, R.J., 1998. High-temperature pressure-shear plate impact experiments on OFHC copper. Journal of the Mechanics and Physics of Solids 46, 1723–1743.

Grady, D.E., Mashimo, T., 1992. Shock and release wave properties of yttria-doped tetragonal and cubic zirconia. Journal of Applied Physics 71, 4868–4874.

Grujicic, M., Pandurangan, B., Cheeseman, B.A., 2006. The effect of degree of saturation of sand on detonation phenomena associated with shallow-buried and ground-laid mines. Shock and Vibration 13, 41–61.

Grujicic, M., Pandurangan, B., Summers, J.D., Cheeseman, B.A., Roy, W.N., Skaggs, R.R., 2008. Application of the modified compaction material model to the analysis of landmine detonation in soil with various degrees of water saturation. Shock and Vibration 15, 77–99.

Grunschel, S.E., Clifton, R.J., 2007. Dynamic plastic response of aluminum at temperatures approaching melt. Metallurgical and Materials Transactions A 38, 2885–2890.

Gupta, Y.M., 1976. Shear measurements in shock-loaded solids. Applied Physics Letters 29, 694–697.

Hill, R., 1950. The Mathematical Theory of Plasticity. Clarendon Press, Oxford, England.

Holmquist, T.J., Johnson, G.R., 2008. The failed strength of ceramics subjected to high-velocity impact. Journal of Applied Physics 104, 013533.

Homae, T., Wakabayashi, K., Matsumura, T., Nakayama, Y., 2007. Reduction of explosive damage using sand or water layer. In: Elert, M., Furnish, M.D., Chau, R., Holmes, N., Nguyen, J. (Eds.), Shock Compression of Condensed Matter - 2007. AIP, pp. 1289–1292.

Housen, K.R., Holsapple, K.A., 2003. Impact cratering on porous asteroids. Icarus 163, 102–119.

Kabir, M.E., Song, B., Martin, B.E., Chen, W., 2010. Compressive behavior of fine sand. Sandia National Laboratories, Report SAND2010-2289.

Kim, K.-S., Clifton, R.J., Kumar, P., 1977. A combined normal- and transverse-displacement interferometer with an application to impact of y-cut quartz. Journal of Applied Physics 48, 4132–4138.

Klopp, R.W., Clifton, R.J., 1990. Analysis of tilt in the high-strain-rate pressure-shear plate impact experiment. Journal of Applied Physics 67, 7171–7173.

Kolsky, H., 1963. Stress Waves in Solids. Dover, New York.

Laine, L., Ranestad, Ø., Sandvik, A., Snekkevik, A., 2002. Numerical simulation of anti-tank mine detonations. In: Furnish, M.D., Thadhani, N.N., Horie, Y. (Eds.), Shock Compression of Condensed Matter - 2001. AIP, pp. 431–434.

Lassner, E., Schubert, W.-D., 1999. Tungsten: Properties, Chemistry, Technology of the Element, Alloys, and Chemical Compounds. Kluwer Academic / Plenum Publishers, N.Y.

Lysne, P.C., 1970. A comparison of calculated and measured low-stress Hugoniots and release adiabats of dry and water-saturated tuff. Journal of Geophysical Research 75, 4375–4386.

Martin, B.E., Chen, W., Song, B., Akers, S.A., 2009. Moisture effects on the high strain-rate behavior of sand. Mechanics of Materials 41, 786–798.

Mitchell, J.K, Soga, K., 2005. Fundamentals of Soil Behavior, 3rd Edition. John Wiley & Sons, Hoboken, N.J.

Nesterenko, V.F., Meyers, M.A., Chen, H.C., 1996. Shear localization in high-strain-rate deformation of granular alumina. Acta Materialia 44, 2017–2026.

Ramesh, K.T., Clifton, R.J., 1987. A pressure-shear plate impact experiment for studying the rheology of lubricants at high pressures and high shearing rates. Journal of Tribology 109, 215–222.

Reinhart, W.D., Thornhill, T.F., 2010. The road to obliquity: the resurrection of the STAR facility's pressure-shear gun. In: Proceedings of the 61st Aeroballistic Range Association Meeting. Thun, Switzerland.

Resnyansky, A.D., Wildegger-Gaissmaier, A.E., 2001. Hydrocode modelling of high-velocity jet penetration into sand. In: Crewther, I.R. (Ed.), 19th International Symposium of Ballistics. RUAG Land Systems, Interlaken, Switzerland, pp. 1561–1567.

Sairam, S., Clifton, R.J., 1994. Pressure-shear impact investigation of dynamic fragmentation and flow of ceramics. In: Gilat, A. (Ed.), Mechanical Testing of Ceramics and Ceramic Composites, AMD Vol. 197. ASME, New York, pp. 23–40.

Shih, C.J., Meyers, M.A., Nesterenko, V.F., 1998a. High-strain-rate deformation of granular silicon carbide. Acta Materialia 46, 4037–4065.

Shih, C.J., Nesterenko, V.F., Meyers, M.A., 1998b. High-strain-rate deformation and comminution of silicon carbide. Journal of Applied Physics 49, 4660–4671.

Shockey, D.A., Marchand, A.H., Skaggs, S.R., Cort, G.E., Burkett, M.W., Parker, R., 1990. Failure phenomenology of confined ceramic targets and impacting rods. International Journal of Impact Engineering 9, 263–275.

Song, B., Chen, W., Luk, V.K., 2009. Impact compressive response of dry sand. Mechanics of Materials 41, 777–785.

Spletzer, S.V., Dandekar, D.P., 2001. Deformation of a low-cost Ti-6Al-4V armor alloy under shock loading. U.S. Army Research Laboratory, Report ARL-TR-2386.

Strand, O.T., Goosman, D.R., Martinez, C., Whitworth, T.L., Kuhlow, W.W., 2006. Compact system for high-speed velocimetry using heterodyne techniques. Review of Scientific Instruments 77, 083108.

Sundaram, S., Clifton, R.J., 1998. Flow behavior of soda-lime glass at high pressures and high shear rates. In: Schmidt, S.C., Dandekar, D.P., Forbes, J.W. (Eds.), Shock Compression of Condensed Matter - 1997. American Institute of Physics, pp. 517–520.

Tang, Z., Aidun, J.B., 2009. Combined compression and shear plane waves. In: Horie, Y. (Ed.), Shock Wave Science and Technology Reference Library. Vol. 3. Springer, Berlin, pp. 109–167.

Vogler, T.J., Lee, M.Y., Grady, D.E., 2007. Static and dynamic compaction of ceramic powders. International Journal of Solids and Structures 44, 636–658.

Vogler, T.J., Thornhill, T.F., Reinhart, W.D., Borg, J.P., 2011. Shock loading of dry and wet sand: Experiments and mesoscale simulations(in preparation).

Yadav, S., Chichili, D.R., Ramesh, K.T., 1995. The mechanical response of a 6061-T6 Al/Al_2O_3 metal matrix composite at high rates of deformation. *Acta Metallurgica et Materialia* **43**, 4453–4464.

Yadav, S., Ramesh, K.T., 1998. The mechanical behavior of polycrystalline hafnium: strain-rate and temperature dependence. Materials Science and Engineering A246, 265–281.

Yuan, F., Liou, N.-S., Prakash, V., 2009. High-speed frictional slip at metal-on-metal interfaces. International Journal of Plasticity 25, 612–634.

Yuan, G., Feng, R., Gupta, Y.M., 2001. Compression and shear wave measurements to characterize the shocked state in silicon carbide. Journal of Applied Physics 89, 5372–5380.

This page intentionally left (almost) blank.

A Tilt

Despite the great care taken to align the projectile nose with the driver plate, some tilt inevitably occurs in plate impact experiments. In most cases (of the first five experiments), the tilt was between 1 and 2.5 mrad (0.05° to 0.14°), though in ps-wc-2 it was 4.5 mrad (0.26°). These angles are quite small and typically have no significant effect upon the results of plate impact experiments. However, in this study we are specifically measuring the transverse motion of the anvil. The reflection of the longitudinal wave, which has some obliquity due to the tilt, from the free surface of the anvil leads to the generation of both longitudinal and shear motion [Kolsky, 1963].

While the tilt angles mentioned above are quite modest and would not generate significant transverse motion, the effective tilt of the longitudinal wave in the target is significantly greater as given by [Klopp and Clifton, 1990]

$$\Phi = \frac{C_L^{anv}}{V_{impact}} \phi, \tag{7}$$

where Φ is the tilt of the longitudinal wave travelling in the anvil, referred to as the effective tilt, and ϕ is the tilt of the impactor. Because we are only concerned with shear motion that will be measured by the VISAR system, we will take ϕ to be the component of tilt in the $x-y$ plane; $x-z$ tilt can be ignored [Klopp and Clifton, 1990]. Examination of Eq. 7 reveals that the effective tilt Φ can be up to two orders of magnitude greater than the projectile tilt ϕ since C_L^{anv} will be significantly greater than the impact velocity in these experiments. The effect is illustrated by images from a 2-dimensional simulation conducted with CTH that are shown in Fig. A.1. Elastic properties for ZrO_2 were used for the materials in the simulation. In the left image, an impactor plate with a velocity of 188 m/s and a tilt of 1.7 mrad (0.1°) is just about to strike a stationary target. At a slightly later time shown in the right image, a shock is travelling outward from the impact plane. From Eq. 7, we find an effective tilt Φ of 63 mrad (3.6°).

To explore the issue further, additional calculations were conducted with CTH in which a ZrO_2 impactor strikes a ZrO_2 driver and anvil with a 100 μm layer of aluminum sandwiched between them. The initial velocity of the impactor is defined so as to be equivalent to a projectile velocity of 200 m/s and 20° obliquity. Values of tilt of -1, 0, 1, 2, and 5 mrad were assumed, and the velocities observed at the free surface of the anvil are shown in Fig. A.2. For the $\phi = 0$ case, the longitudinal wave arrives at about 1 μs, and the transverse wave with an amplitude of about 15.6 m/s arrives slightly over a microsecond later. The amplitude of the shear wave corresponds to a shear stress in the Al sample of 0.17 GPa (Eq. 4), which is consistent with the flow stress Y used in the simulations of 0.30 GPa (Eq. 6). For non-zero values of tilt, the longitudinal wave arrives later since $t = 0$ represents the time of initial impact but the measurements are shown for the center of the model; thus, the time delay of the longitudinal wave is merely proportional to the tilt and the height of the model. When there is tilt, there is also non-zero transverse velocity at the time of the longitudinal wave arrival. As stated before, this is due to the reflection of the oblique normal wave from the free surface of the anvil. In all cases, though, slightly more than 1 μs later the shear wave arrives, and the transverse velocity goes to the same equilibrium value of 15.6 m/s seen for the zero tilt case. Thus, one can conclude that the presence of tilt, even though the effective tilt might be relatively large, will not effect the equilibrium value of the transverse velocity.

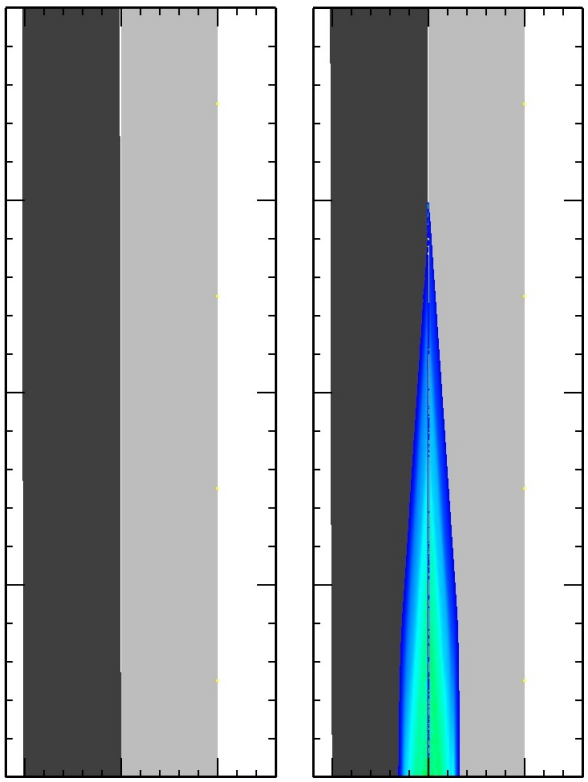

(a) **(b)**

Figure A.1. Contour plots of CTH simulations of impact with tilt of 0.1° at (a) initial impact and (b) 0.2 μs later.

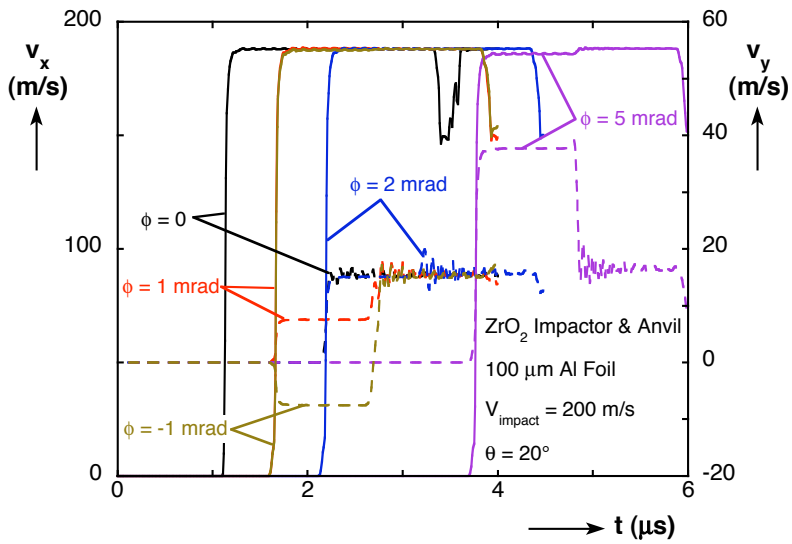

Figure A.2. Longitudinal velocity v_x (solid lines) and transverse velocity v_y (dashed lines) at the free surface of the anvil from CTH simulations with varying amounts of tilt.

While tilt was measured in all experiments, in two experiments the orientation of the tilt pins relative to the $y-z$ plane was not recorded. For the remainder, the transverse velocity v_y due to tilt is normalized by the longitudinal free surface velocity since the analytic solution shows the transverse velocity generated by an incoming wave with tilt is proportional to the amplitude of the wave. The data are plotted against the effective tilt in Fig. A.3 along with the analytic solution from Kolsky [1963] and the results from CTH simulations as outlined above with or without the aluminum layer. The CTH results agree well with the analytic solution, albeit with slight deviations at higher tilts. Since the analytic solution is based on a small strain assumption, some differences are not surprising. The experimental results also agree very well with both the analytic and simulation results. Thus, it can be concluded that the early-time transverse motion is due to tilt of the impactor.

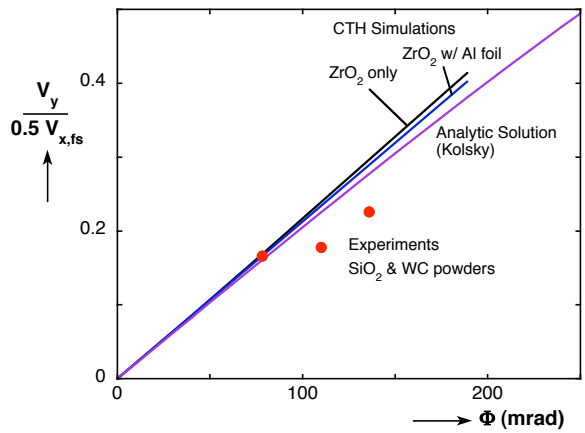

Figure A.3. Transverse velocity amplitude due to tilt relative to the effective tilt angle of the propagating wave Φ in the experiments. Also shown for comparison are the analytical solution of Kolsky [1963] and the results of two-dimensional calculations with CTH.

B VISAR Records

In this section the raw and resolved velocity records for the experiments are shown. Records are shown for all of the experiments except for two where the velocity records were of very poor quality or a velocity record was not obtained. Some of these plots have been shown in previous sections, but they are included here for completeness.

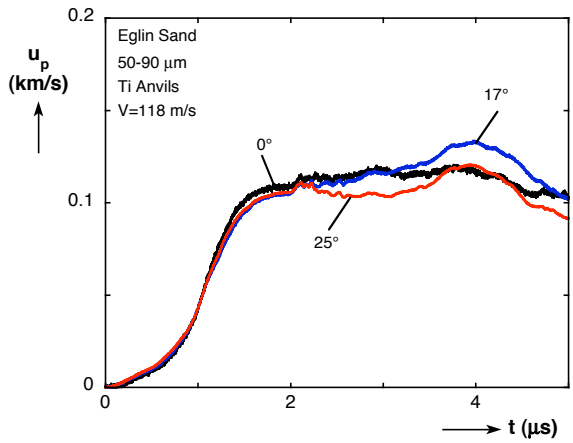

(a)

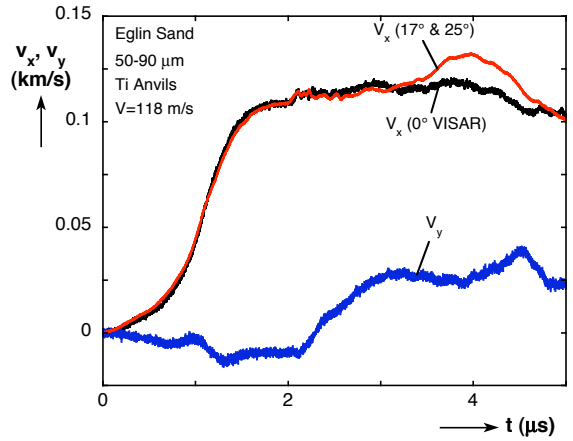

(b)

Figure B.4. Velocity measurements for experiment ps-egs-1 as (a) raw measurements from normal (0°) and off-axis (17° and 25°) probes and (b) resolved velocities for the normal and transverse directions. The time scale has been shifted so that the longitudinal wave arrives at the free surface at $t = 0$.

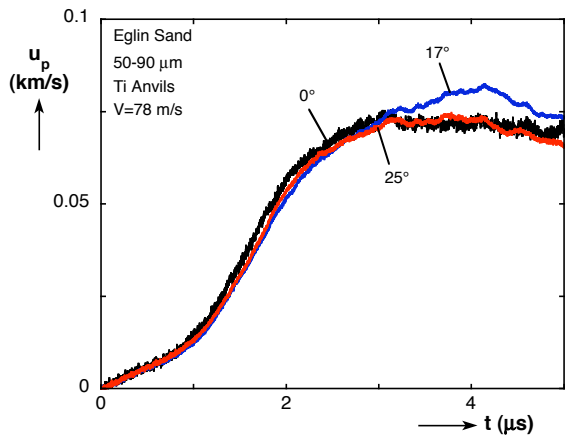

(a)

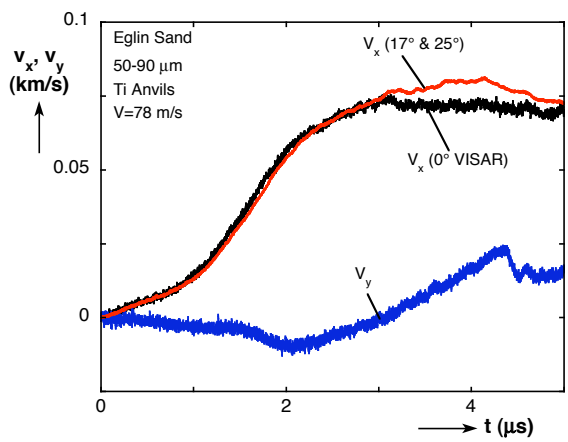

(b)

Figure B.5. Velocity measurements for experiment ps-egs-2 as (a) raw measurements from normal (0°) and off-axis (17° and 25°) probes and (b) resolved velocities for the normal and transverse directions. The time scale has been shifted so that the longitudinal wave arrives at the free surface at $t = 0$.

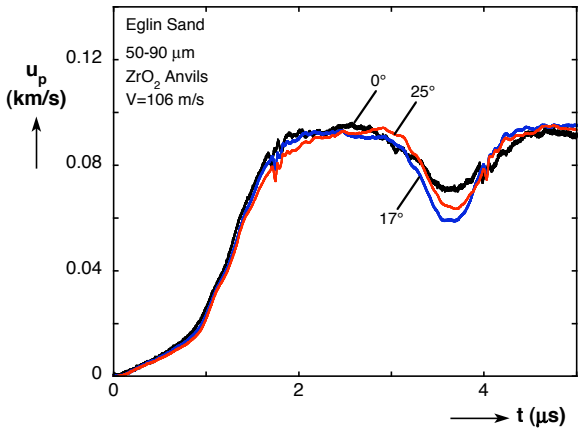

(a)

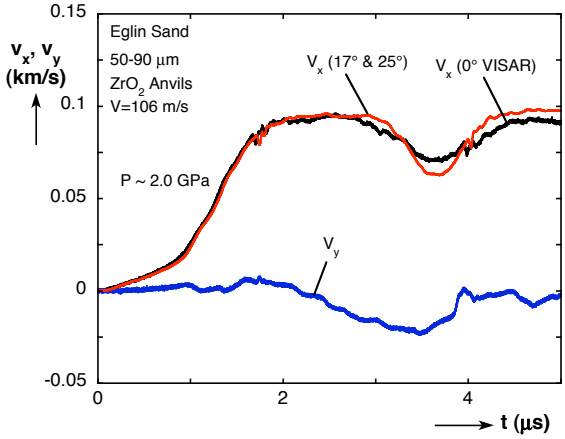

(b)

Figure B.6. Velocity measurements for experiment ps-egs-3 as (a) raw measurements from normal (0°) and off-axis (17° and 25°) probes and (b) resolved velocities for the normal and transverse directions. The time scale has been shifted so that the longitudinal wave arrives at the free surface at $t = 0$.

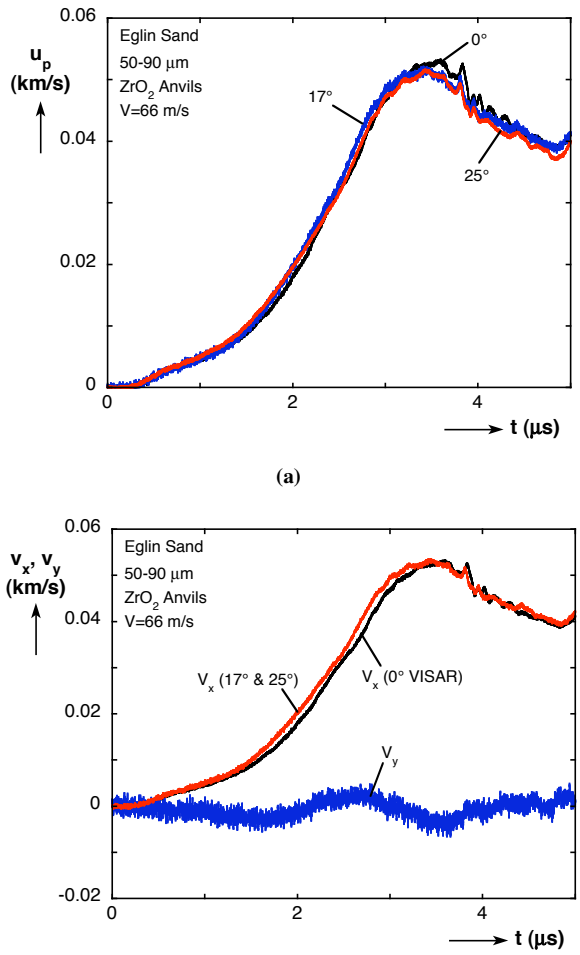

Figure B.7. Velocity measurements for experiment ps-egs-5 as (a) raw measurements from normal (0°) and off-axis (17° and 25°) probes and (b) resolved velocities for the normal and transverse directions. The time scale has been shifted so that the longitudinal wave arrives at the free surface at $t = 0$.

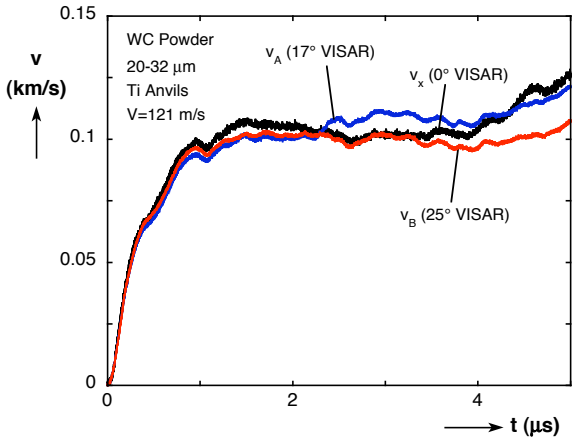

(a)

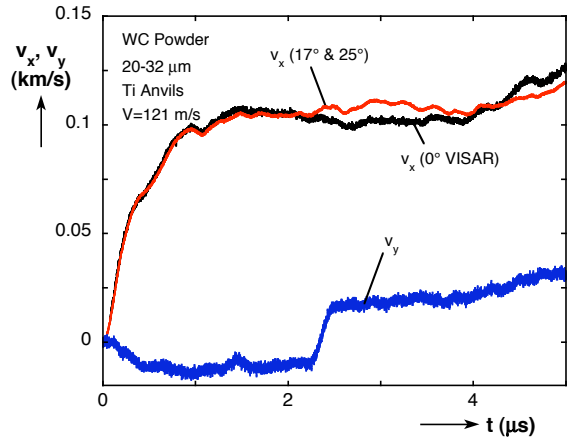

(b)

Figure B.8. Velocity measurements for experiment ps-wc-1 as (a) raw measurements from normal (0°) and off-axis (17° and 25°) probes and (b) resolved velocities for the normal and transverse directions. The time scale has been shifted so that the longitudinal wave arrives at the free surface at $t = 0$.

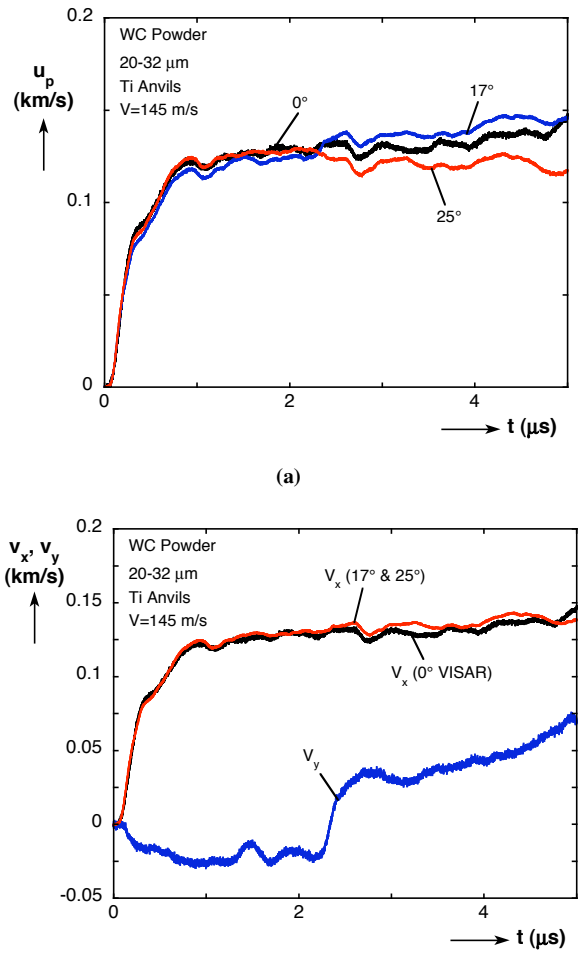

Figure B.9. Velocity measurements for experiment ps-wc-2 as (a) raw measurements from normal (0°) and off-axis (17° and 25°) probes and (b) resolved velocities for the normal and transverse directions. The time scale has been shifted so that the longitudinal wave arrives at the free surface at $t = 0$.

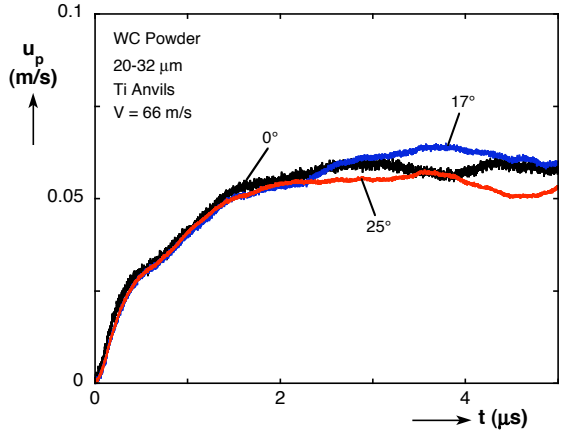

(a)

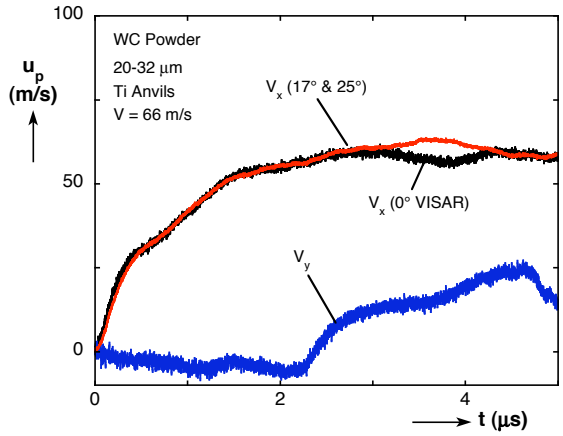

(b)

Figure B.10. Velocity measurements for experiment ps-wc-3 as (a) raw measurements from normal (0°) and off-axis (17° and 25°) probes and (b) resolved velocities for the normal and transverse directions. The time scale has been shifted so that the longitudinal wave arrives at the free surface at $t = 0$.

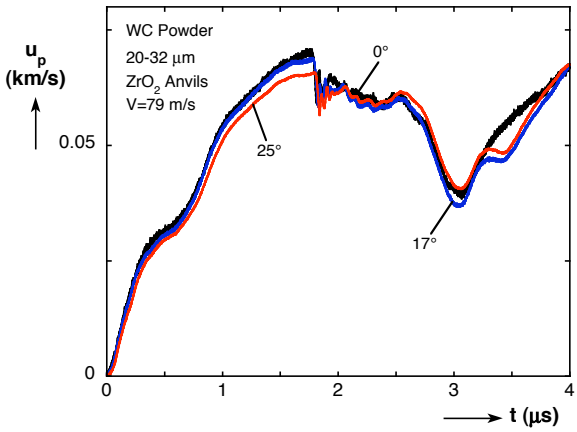

(a)

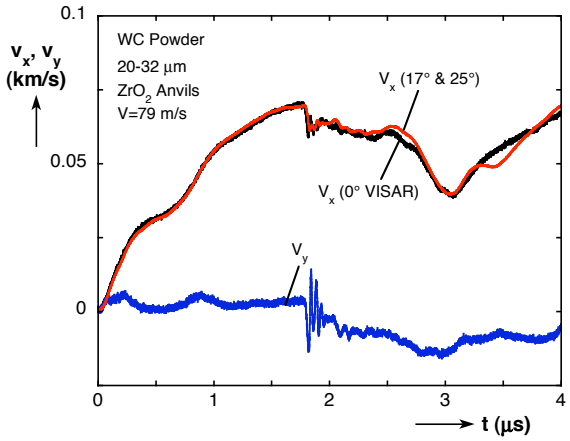

(b)

Figure B.11. Velocity measurements for experiment ps-wc-4 as (a) raw measurements from normal (0°) and off-axis (17° and 25°) probes and (b) resolved velocities for the normal and transverse directions. The time scale has been shifted so that the longitudinal wave arrives at the free surface at $t = 0$.

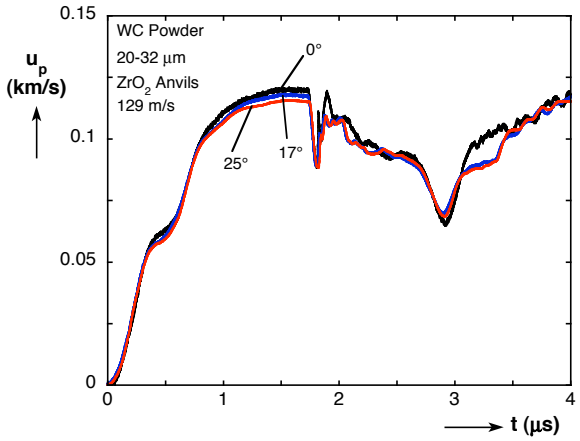

(a)

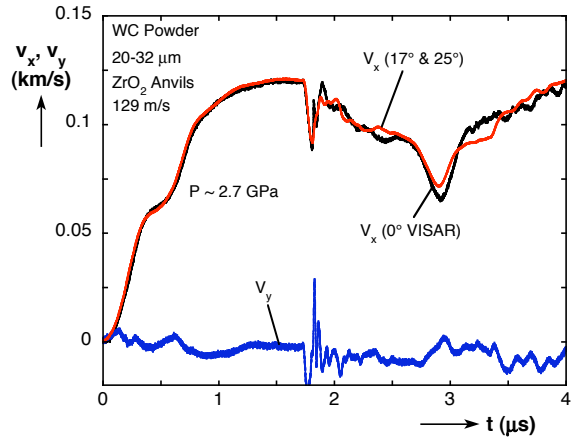

(b)

Figure B.12. Velocity measurements for experiment ps-wc-6 as (a) raw measurements from normal (0°) and off-axis (17° and 25°) probes and (b) resolved velocities for the normal and transverse directions. The time scale has been shifted so that the longitudinal wave arrives at the free surface at $t = 0$.

DISTRIBUTION:

1 Don Cargile
CEERD-GM-1
3909 Halls Ferry Road
Vicksburg, MS 39180

1 Danny Hayles
DTRA / CXWW
Bldg. 13A, Suite 392
101 W. Eglin
Eglin AFB, FL 32542

1 Mark Green
Air Force Research Laboratory
101 West Eglin Blvd, Suite 135
Eglin AFB, FL 32542-6810

1 Lalit Chhabildas
Air Force Research Laboratory
101 West Eglin Blvd, Suite 135
Eglin Air Force Base, FL 32542

1 William Cooper
Air Force Research Laboratory
101 West Eglin Blvd, Suite 135
Eglin AFB, Fl 32542

1 Müge Fermen-Coker
U.S. Army Research Laboratory
Aberdeen Proving Ground, MD 21005

1 Dan Casem
U.S. Army Research Laboratory
RDRL-WMP-B
Aberdeen Proving Ground, MD 21005

1 Tarabay Antoun
Lawrence Livermore National Laboratory
7000 East Avenue
Livermore, CA 94550

1 Don Fujino
Lawrence Livermore National Laboratory
7000 East Avenue
Livermore, CA 94550

1 Ilya Lomov
Lawrence Livermore National Laboratory
7000 East Avenue
Livermore, CA 94550

1 Efrem Vitali
Lawrence Livermore National Laboratory
7000 East Avenue
Livermore, CA 94550

1 Jeff Florando
Lawrence Livermore National Laboratory
7000 East Avenue
Livermore, CA 94550

1 Dana Dattelbaum
Los Alamos National Laboratory
P.O. Box 1663
Los Alamos, NM 87545

1 Darcie Dennis-Koller
Los Alamos National Laboratory
P.O. Box 1663
Los Alamos, NM 87545

1 D. Anthony Fredenburg
Los Alamos National Laboratory
P.O. Box 1663
Los Alamos, NM 87545

1 Rick Gustavsen
Los Alamos National Laboratory
P.O. Box 1663
Los Alamos, NM 87545

1 Brian Jensen
Los Alamos National Laboratory
P.O. Box 1663
Los Alamos, NM 87545

1 Rick Martineau
Los Alamos National Laboratory
P.O. Box 1663
Los Alamos, NM 87545

1 David Robbins
Los Alamos National Laboratory
P.O. Box 1663
Los Alamos, NM 87545

1 Tim Holmquist
Southwest Research Institute
5353 Wayzata Blvd
Minneapolis, MN 55416

1 Charley Anderson
Southwest Research Institute
P.O. Drawer 28510
San Antonio, TX 78228-0510

1 Don Shockey
SRI International
333 Ravenswood Ave.
Menlo Park, CA 94025

1 John Foster
The University of Texas at San Antonio
EB 3.04.22
One UTSA Circle
San Antonio, TX 78249

1	MS 1164	P.C. Butler, 5435
1	MS 1205	C.A. Hall, 5947
1	MS 1160	D. Burnett, 5431
10	MS 9042	T.J. Vogler, 8246
1	MS 9042	Chris Moen, 8246
1	MS 9154	M.E. Gonzales, 8240
1	MS 1186	M. Herrmann, 1640
1	MS 1106	T. Ao, 1646
1	MS 1195	C.S. Alexander, 1646
1	MS 1195	J.-P. Davis, 1646
1	MS 1195	D. Dolan, 1646
1	MS 1186	D. Flicker, 1646
1	MS 1195	M.D. Furnish, 1646
1	MS 1195	R.J. Hickman, 1647
1	MS 1195	M.D. Knudson, 1646
1	MS 1195	G.T. Leifeste, 1647
1	MS 1195	J. Robbins, 1646
1	MS 1195	S. Root, 1646
1	MS 1195	W.D. Reinhart, 1646
1	MS 1195	T.F. Thornhill, 1647
1	MS 1195	J.L. Wise, 1646
1	MS 0899	Technical Library, 9536 (electronic copy)

This page intentionally left (almost) blank.

Sandia National Laboratories